Composite Norland Optical Adhesive (NOA)/silicon flow focusing devices for colloidal particle manipulation and synthesis

Naval Singh, Adnan Chakra, Goran Vladisavljević, Cécile Cottin-Bizonne, Christophe Pirat, Guido Bolognesi

NOA-silicon flow focusing devices for colloidal particle manipulation and synthesis

Naval Singh, Adnan Chakra, Goran Vladisavljević, Cécile Cottin-Bizonne, Christophe Pirat, Guido Bolognesi

Composite Norland Optical Adhesive (NOA)/silicon flow focusing devices for colloidal particle manipulation and synthesis

Naval Singh[a], Adnan Chakra[a], Goran T. Vladisavljević[a], Cécile Cottin-Bizonne[b], Christophe Pirat[b], Guido Bolognesi[a,*]

[a] *Department of Chemical Engineering, Loughborough University, Loughborough, LE11 3TU, United Kingdom*

[b] *Institut Lumière Matière, UMR5306 Université Claude Bernard Lyon 1 - CNRS, Université de Lyon, Villeurbanne Cedex, 69622, France*

Abstract

Microfluidic flow focusing devices are widely used to generate steep chemical concentration gradients at the interface between miscible or partially miscible streams. In this study, first we present an optimised protocol for the manufacturing of composite flow focusing devices, consisting of a micropatterned layer of Norland Optical Adhesive (NOA) glue bound to flat or microgrooved silicon substrates. Then, three different applications of these devices are demonstrated, namely (i) particle spreading and focusing in continuous flows past flat substrates, (ii) particle accumulation within the dead-end cavities of microgrooved substrates and (iii) synthesis of nano-sized liposomes. Colloidal particle spreading, focusing and accumulation were achieved through diffusiophoresis transport induced by salt concentration gradients at the interface between electrolyte streams. Epi-fluorescence microscopy was adopted to characterise the spatiotemporal distribution of silica and polystyrene nanoparticles in the devices with flat or microgrooved surfaces. The effects of particle zeta potential and groove thickness on particle dynamics were investigated. 1,2-di-(9Z-octadecenoyl)-sn-glycero-3-phosphocholine (DOPC) liposomes were generated by hydrodynamic focusing and characterised via dynamic light scattering. Liposome populations with controlled narrow size distributions could be achieved by adjusting the flow rate conditions in the devices. This work demonstrates that composite NOA-silicon flow junction devices offer a competitive alternative to conventional PDMS chips and can support a wide range of microfluidic applications, including nanoparticle synthesis, characterisation and filtration, drug encapsulation and biochemical analysis.

Keywords: microfabrication, NOA, silicon, flow focusing, microfluidics, diffusiophoresis, liposomes

*Corresponding author
Email address: g.bolognesi@lboro.ac.uk (Guido Bolognesi)

1. Introduction

Microfluidic devices play a pivotal role in many physical, chemical, biological and engineering applications relevant to both research and commercial use [1]. The choice of the device material and fabrication method is a crucial step that can determine the overall viability of the proposed microfluidic application. The first generation of microfluidic chips were prepared in glass and silicon, as these materials were traditionally used by the molecular analysis and microelectronic industries [2, 3, 4]. Due to their many key advantages, as excellent solvent compatibility, high thermoconductivity, good surface stability, high elastic modulus and stable electroosmotic mobility, glass and silicon are still widely used in microfluidic research [5, 6, 7, 8, 9]. Since silicon is transparent to infrared but not to visible light, glass devices are usually preferred when optical access to the flow is required, such as in fluorescence detection or fluid imaging. Alternatively, silicon microchannels can be bound to a transparent material (glass or polymer), thereby resulting in a composite device with optical access from one side only.

Over the past decades, many pioneering studies have introduced microfluidic fabrication methods using polymers and some of these methods (e.g. hot embossing, injection moulding) are relatively inexpensive and more easily scalable for large production [10, 11]. In laboratory settings, the most accustomed polymer is certainly polydimethylsiloxane (PDMS) because of its many excellent physical and chemical properties. PDMS devices have good chemical and thermal stability, are easy to functionalise via physical or chemical surface treatments, are optically transparent, gas permeable, mechanically resistant, and soft enough to allow the integration of active flow control elements (e.g. valves and pumps). Also, the numerous PDMS-based soft-lithography techniques, developed over the years [12, 13], made this elastomeric polymer a standard tool of many microfluidic research laboratories. Since the seminal work by Bartolo et al. [14], optically transparent and chemically-resistant photocurable polymers, such as Norland Optical Adhesive (NOA) glues, have been increasingly used for microfluidic device fabrication due to their excellent optical transparency, chemical resistance to many organic solvents, impermeability to gases and water vapour, and relatively high elastic modulus that prevents channel deformation under high pressure flows. NOA devices can be fabricated via a soft-lithography process, called microfluidic sticker technique [14], which also allows the manufacturing of composite devices made of NOA and another gas-impermeable substrate (e.g. glass, silicon). Notably, the NOA components of these composite devices can be dissolved in chlorinated solvents, thereby enabling the recovery of the other substrates after device use.

Flow focusing channel design, where an inner channel meets two outer channels at a junction, has been extensively used in several microfluidic applications [15, 16, 17]. When two immiscible streams (like water and oil) meet at a flow focusing junction, the high shear stress can mediate the interfacial tension-driven destabilisation of the liquid-liquid interface and lead to the controlled production of emulsion droplets and microparticles [17, 18]. Alternatively, when

the two streams are miscible or partially miscible, the flow focusing configuration can be exploited to create narrow diffusion layers with steep chemical concentration gradients at the interface between the two streams. The mixing of chemicals in the diffusion layer can trigger chemical reactions or physicochemical responses, leading to the synthesis of nanoparticles under continuous flow settings [19, 20]. For instance, hydrodynamic flow focusing has been adopted to produce narrow-sized populations of liposomes, micelles and metallic nanoparticles, encapsulating drugs or other active ingredients [21, 22, 23, 24]. Furthermore, chemical gradients in flow focusing devices can be exploited to induce the spontaneous migration of colloidal particles along the streamlines of the chemical gradient field, a phenomenon referred to as diffusiophoresis [25, 26]. By relying on this phoretic transport mechanism, flow focusing devices generating salt concentration gradients have been developed to achieve colloidal particle spreading, focusing, filtration and accumulation [27, 28, 29].

In this study, we report the optimised protocol for the fabrication of composite NOA flow focusing devices bound to flat and microgrooved silicon substrates. Three different applications of these devices are demonstrated, namely (i) particle spreading and focusing on flat substrates, (ii) particle accumulation within the grooves of microstructured substrates and (iii) synthesis of liposomes with controlled narrow size distributions. Our results demonstrate the potential of NOA flow focusing devices as a valuable tool for supporting fundamental research in physics and chemistry as well as underpinning a wide range of microfluidic applications, such as nanoparticle synthesis, filtration and characterisation, drug encapsulation and bioanalysis. Hence, this work will further encourage the interdisciplinary uptake of NOA microfluidics by the scientific community and consolidate its role as a competitive alternative to conventional PDMS microfluidics.

2. Experimental

2.1. Materials

Negative photoresist SU-8-2050 (MicroChem Corp.) and photoresist developer (EC-Solvent) were purchased from A-Gas Electronic Materials. Polydimethylsiloxane (PDMS) (Momentive RTV615 A+B-Kit, base + curing agent) was purchased from Techsil, and the photoreactive adhesive Norland Optical Adhesive 81 (NOA 81) from Norland Products Inc. The silicon microgrooved substrates were fabricated via Deep Reactive Ion Etching (DRIE) by MIMENTO (MIcrofabrication for MEcanics, Nanosciences, Thermal and Optics) technology centre, hosted by FEMTO-ST Institut in Besançon, France. The substrates had transverse grooves, 24 µm wide and 45 µm deep, evenly spaced 32 µm apart over a 4 cm long region. The rectangular flat silicon surfaces, used for the fabrication of the flat microchannels, were manually cut from four inch diameter silicon wafers, purchased from Inseto.

The fluorescent silica nanobeads (0.05% solids w/v) were purchased from the Kisker Biotech GmbH & Co.KG company, and the fluorescent polystyrene nanobeads (FluoSpheres^{TM}, 1.02% solids w/v) were purchased from Thermo Fisher

Scientific. All colloidal nanobeads have a nominal diameter of 200 nm. The lithium chloride salt (LiCl, 99%) was purchased from Acros Organics. TRIS hydrochloride, ethylenediaminetetraacetic acid (EDTA) (98.5%), HEPES (99.5%) and ethanol 1 2-di-(9Z-octadecenoyl)-sn-glycero-3-phosphocholine (DOPC) were purchased from Sigma-Aldrich. All aqueous solutions were prepared using DI water of resistivity 18.2 MΩcm from an Ultrapure Milli-Q grade purification system (Millipore, USA). The chlorinated solvent, dichloromethane (anhydrous, $\geq$ 99.8%) chloroform (anhydrous, $\geq$ 99%), methanol (anhydrous, 99.8%) and ammonium hydroxide, used for recovery of the microgrooved substrate, were purchased from Sigma-Aldrich.

2.2. Particle characterisation

Dynamic light scattering and electrophoretic light scattering measurements were performed to determine average particle size and zeta potential of colloidal particles, respectively. A Delsa^{TM} Nano Zeta Potential and Submicron Particle Size Analyzer by Beckman Coulter provided an average particle size of silica nanoparticles of 205 ± 8 nm and a zeta potential of -41.7 ± 4 mV in 1 mM TRIS buffer (pH=9). Polystyrene particles were characterised in 0.1 mM LiCl solution with a Malvern ZetaSize Nano ZS, providing an average particle size of 207 ± 7 nm and a zeta potential of -58.5 ± 1 mV. Size distribution of the liposomes, manufactured in the microfluidic devices, were also measured with the Malvern ZetaSizer Nano ZS. Note that for zeta potential measurements the instruments provided the zeta potential values calculated according to the Smoluchowski's theory for which the Debye length is much smaller than the particle size. The zeta potential values were corrected to account for the finite size of the Debye length according to Henry's model [30].

2.3. Microfabrication

SU-8 masters were fabricated via contact printing photolithography by means of a UV-KUB 2 (Kloé) exposure and masking system. AutoCAD (Autodesk) software was used for photomask design and high resolution film photomasks were printed by Micro Lithography Services Ltd. A Pluvex 1410 UV exposure unit (Mega Electronics Ltd) was used for the curing of the NOA-81 adhesive. NanoPort assemblies (N-333, Kinesis, Cole-Parmer Ltd) and FEP tubing (Fisher Scientific) were used for connecting the syringes to the inlets of the microfluidic devices.

2.4. Fluorescence microscope analysis

Syringe pumps (Harvard Pump 11 Elite) were used to inject the desired solutions within the microfluidic devices. For particle manipulation experiments, epi-fluorescence images of the particles were acquired via a Nikon Eclipse TE-300 inverted microscope, fitted with a led lamp (CoolLED pE-300), a CMOS camera (Ximea MQ013MG-ON) and a 10x (0.25 NA) objective. The excitation/emission peaks of the particles are 485/510 nm for silica beads and 542/612 nm for polystyrene beads. A filter cube (Nikon B-2A) with 450-490 nm

excitation bandwidth and 515 nm longpass emission filter was used for the visualisation of the silica. A filter cube (Nikon G-2A) with 510-560 nm excitation bandwidth and 590 nm longapass emission filter was used for imaging the polystyrene particles. The TIFF images, acquired by the camera, were processed and analysed via custom Python code. A fluorescence intensity I vs nanoparticle concentration n calibration curve was acquired to ensure that $I \propto n$ for any value of n examined in the experiments.

3. Results and Discussion

3.1. Optimised protocol for the fabrication of microfluidic devices

The Ψ-shaped microchannels were fabricated by means of the microfluidic sticker technique [14]. A flow diagram of the process is shown in Figure 1. Here we report the optimised fabrication protocol which was developed through experimental trial and error. A SU-8 photoresist master was fabricated on a silicon wafer via standard photo-lithography technique. The CAD design of the photomask is shown in Figure 2. The width, w, of the main channel is 400 μm. A PDMS stamp (ca. 6 mm in thickness) was produced from the SU-8 master via replica moulding (Steps 1,2). A 250 μL drop of NOA-81 was then sandwiched between the PDMS stamp and a flat PDMS slab (ca. 4 mm in thickness), so that the glue could spread evenly and uniformly due to the weight of the slab (Step 3). The NOA-81 layer was then exposed to UV light (ca. 365 nm) for 75 seconds at an intensity of 3 mW/cm^2. The exposure time was carefully chosen in order to cure the glue layer, except for the thin glue films in contact with the PDMS slab and stamp, as shown in Figure 1. It should be noted that, since RTV 615 PDMS absorbs UV light slightly, the optimal UV exposure time depends on the thickness of the PDMS slab. Therefore, using a slab of different thickness would require to adjust the exposure time accordingly. After UV exposure, the PDMS stamp must be peeled off (Step 5), so that the partially cured and adhesive NOA layer can be glued onto another substrate. By testing the peeling step with PDMS stamps and slabs of different thicknesses – varying within a range from 3 mm to 6 mm – it was observed that the adhesion between the NOA and PDMS layer was affected by the bending rigidity of the PDMS slab and stamp. Specifically, during peeling, the NOA-81 remains attached to the PDMS layer with the lower bending rigidity and, thus, with the smaller thickness. Consequently, to ensure that the PDMS stamp — and not the slab — is peeled off from the NOA layer, the PDMS stamp must be thicker than the PDMS slab. Once the PDMS stamp was removed, the device inlets and outlet were punched carefully on the imprinted NOA layer, laid on the PDMS slab, by means of a 1 mm diameter biopsy punch (Step 5). Punching the inlet/outlet holes on the NOA layer allows one not to drill the silicon substrates, which are fragile and can easily break. The punched NOA layer was then pressed against a silicon substrate, either flat or with microgrooves, heated to 60°C by a hot plate (Step 6). Heat prevents the formation of air bubbles upon contact between the silicon substrate and the NOA layer. Heat also promotes a weak adhesion

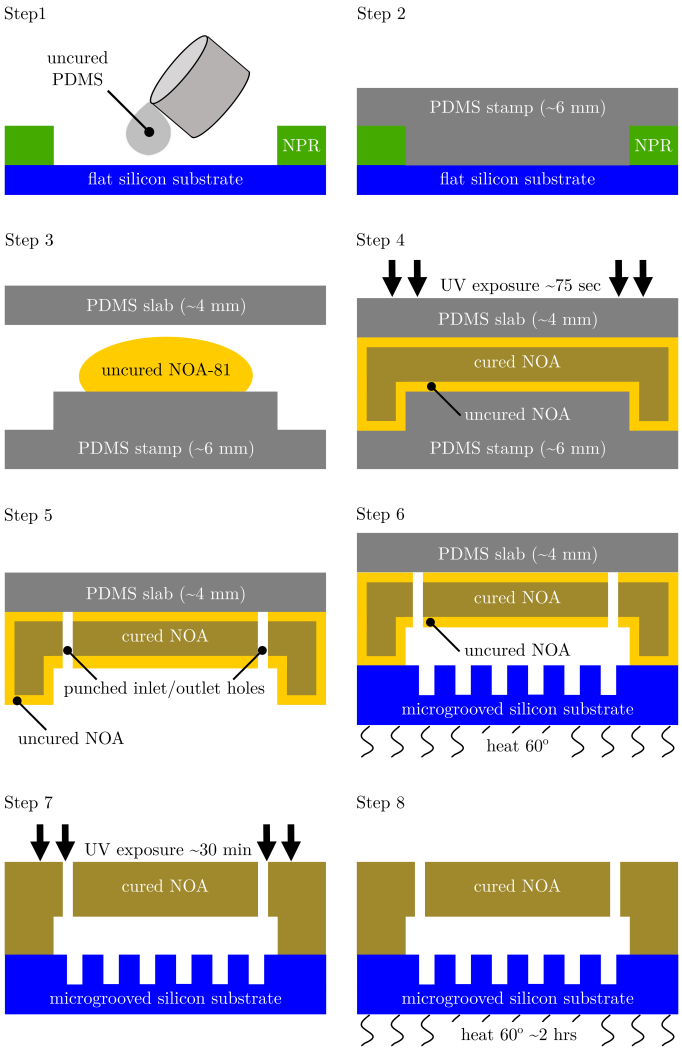

Figure 1: Protocol for the fabrication of a NOA-81 microchannel on a microgrooved silicon substrate via microfluidic sticker technique. Steps 1-2: fabrication of a PDMS stamp, ca. 6 mm in thickness, via replica moulding from a photo-lithographically patterned negative photoresist (NPR). Step 3: spreading of a NOA-81 drop between the PDMS stamp and a PDMS slab (ca. 4 mm in thickness). Step 4: partial curing of the NOA-81 microchannel imprint via UV exposure. Step 5: removal of the PDMS stamp and punching of the inlet/outlet holes. Step 6: deposition of the NOA-81 microchannel on a microgrooved silicon substrate heated on a hot plate. Step 7-8: adhesion of the NOA-81 microchannel on the silicon substrate via UV exposure and heating.

between the silicon and the uncured NOA film, that allows one to peel of the PDMS slab. Note, that it is also possible to punch the inlet/outlet holes at this time, after the PDMS slab is removed, rather than at step 5. However, the NOA

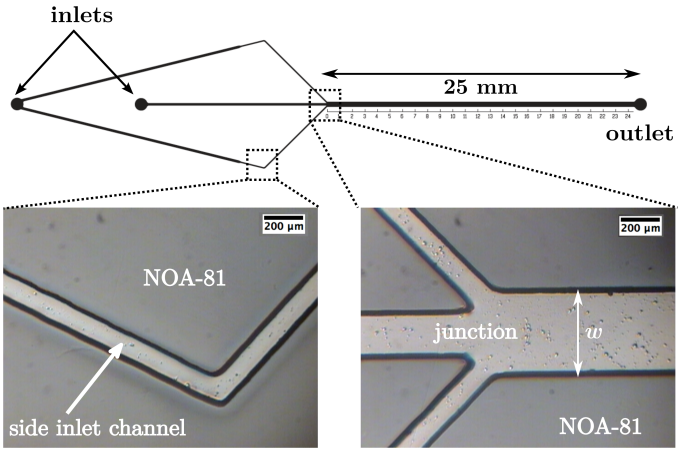

Figure 2: CAD drawing of the photo-lithography mask, and optical micrographs of the NOA-81 microfluidic device at the side inlet channel (left) and at the junction (right). The width, w, of the main channel is 400 µm.

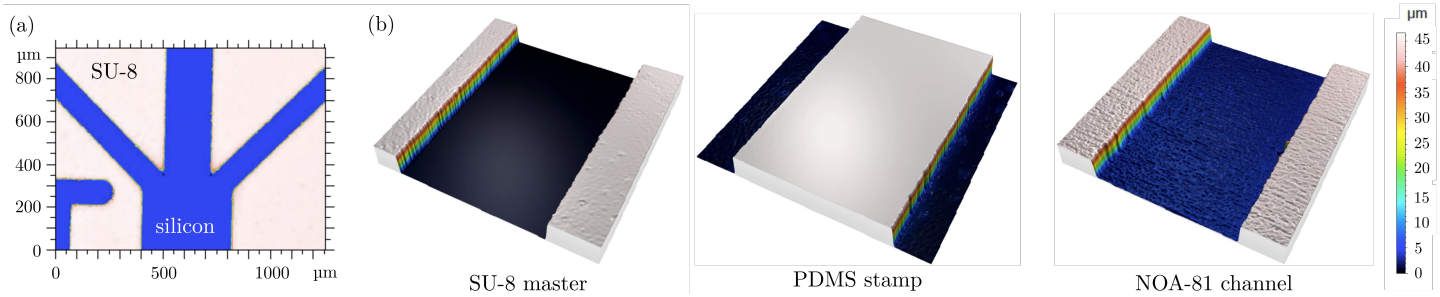

Figure 3: (a) Top-view of the optical profile scan of the SU-8 coated silicon master at the microchannel junction. (b) Axonometric views of the optical profile scans of the SU-8 master, PDMS stamp and NOA-81 microchannel.

microchannel is now laying on the silicon substrate so the puncher should be handled carefully to avoid the breaking of the fragile silicon surface. Finally, the device was exposed to UV light for 30 minutes at an intensity of 3 mW/cm^2 (Step 7) and heated to 60°C on a hot plate for two hours to strengthen the adhesion between NOA layer and silicon substrate (Step 8). Optical micrographs of the final device are shown in Figure 2, whereas 3D optical profiles of the SU-8 master, the PDMS stamp and the NOA-81 channel are shown in Figure 3. The measured depth, h, of the main channel is ca. 45 µm.

Since cured NOA can be dissolved by chlorinated solvents, it is possible to recover the silicon substrates after device use. This feature is very important when expensive substrates, such as DRIE-fabricated silicon surfaces, are used, so that the substrates can be re-used several times and with different channel geometries. After use, the NOA-81 devices were immersed in a chloroform bath

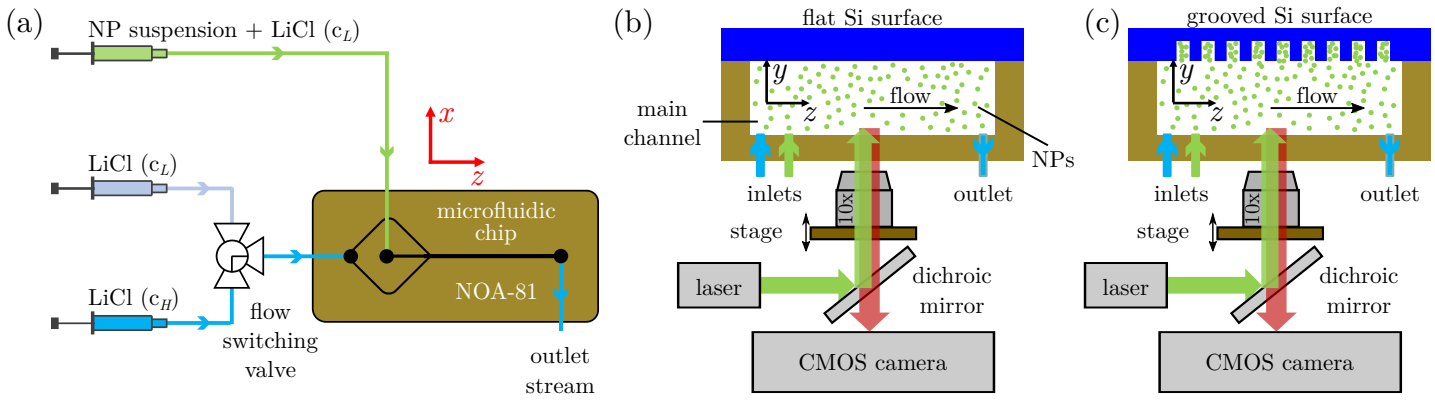

Figure 4: (a) Schematic of the microfluidic set-up. A flow switching valve was used to create a steady-state salt concentration gradient in the flow focusing Ψ-junction device by switching the side streams between LiCl solutions at low (c_L) and high (c_H) concentration. The central stream consisted of nanoparticle (NP) suspension at low salt concentration. (b-c) Schematics of the epifluorescence microscope rig used for the visualisation of the particle distribution in the microfluidic devices fitted with either a flat or microgrooved silicon (Si) surface.

within a sealed glass container for 4-6 hours to remove the cured NOA. Afterwards, the silicon substrates were recovered, rinsed with water and dried with a nitrogen stream. Fluorescent microscope observations of the silicon surfaces after treatment showed that cured NOA was effectively removed, but fluorescent silica and polystyrene nanoparticles were still contaminating the surfaces. The contaminated silicon substrates were then washed in a solution of dichloromethane (100 parts by weight), methanol (15 parts by weight) and 34% ammonium hydroxide aqueous solution (2 parts b weight) at 60°C. Fluorescent microscope analysis confirmed the treatment efficacy in removing polystyrene nanoparticles from the silicon surfaces. Note that the same treatment is less effective for silica nanoparticles, since polystyrene can be dissolved in chlorinated solvents whereas silica can not.

3.2. Particle spreading and focusing on flat substrates

Steady-state salt concentration gradients were generated inside the microfluidic devices to achieve the spreading and focusing of silica and polystyrene nanoparticles by diffusiophoresis, according to a previously reported microfluidic strategy [27, 29]. Previous studies adopted composite PDMS/glass flow focusing devices for generating salt concentration gradients and manipulating the particles via diffusiophoresis. This study is the first to report the use of composite NOA/silicon flow focusing devices for the spreading and focusing of nanoparticles on flat substrates. A schematic of our microfluidic set-up is shown in Figure 4a. To generate the steady-state salt concentration gradients, parallel flows of electrolyte solutions of different ionic strengths were injected by syringe pumps into a Ψ-shaped microchannel, at equal flow rates of 12.5 µL/min. This corresponds to an average velocity within the channel of 23.1 mm/s, calculated

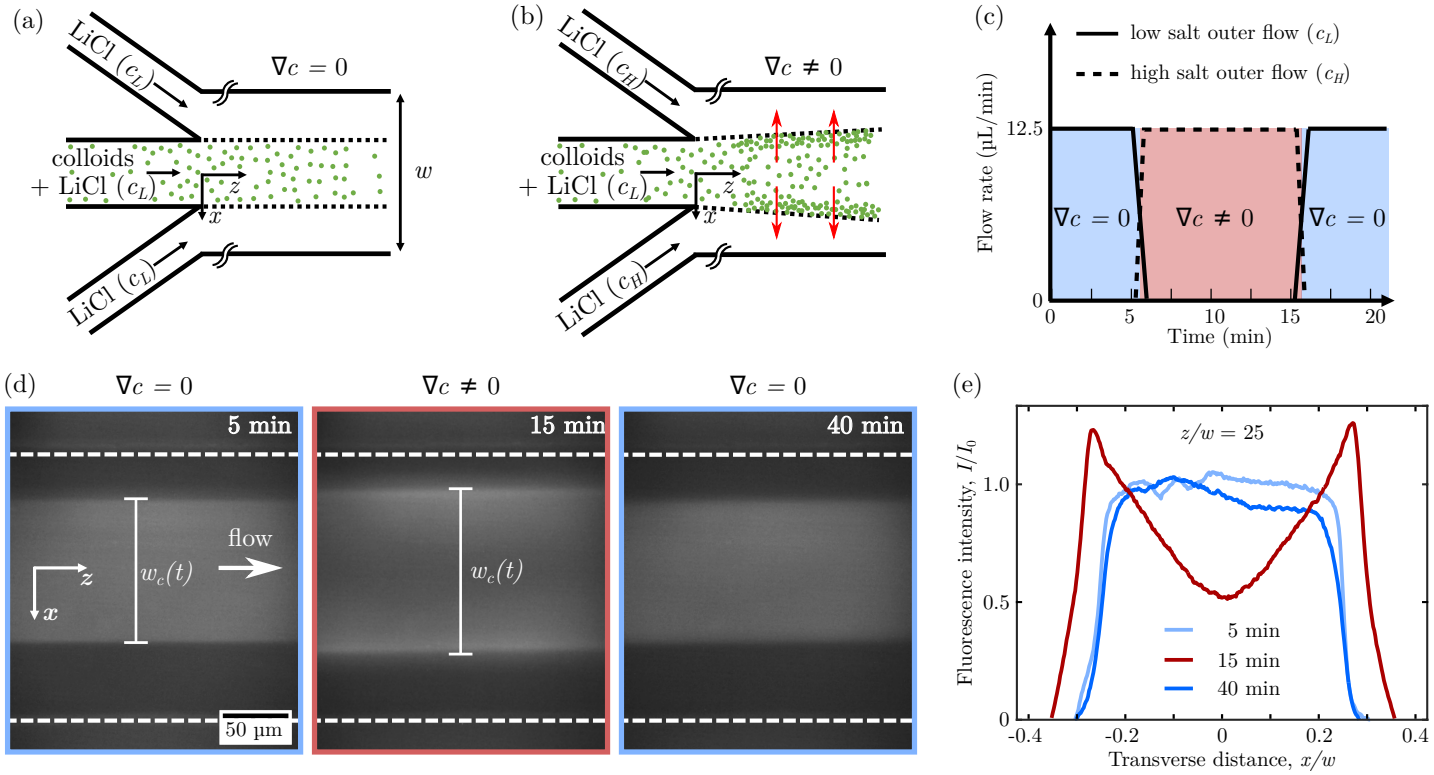

Figure 5: Diffusiophoresis-driven focusing of 200 nm diameter silica particles (0.005% v/v) in a NOA-81 Ψ-junction device with a flat silicon surface. (a-b) Flow configuration in the Ψ-junction device in absence (a) and presence (b) of a steady salt concentration gradient. (c) Time-evolution of the flow rates of the low and high salt outer streams, achieved via the flow switching valve. The red (blue) shaded regions correspond to the presence (absence) of the steady salt concentration gradient, ∇c. (d) Epi-fluorescence micrographs of the main channel at 10 mm ($z/w = 25$) downstream of the junction, before ($t = 5$ min), during ($t = 15$ min) and after ($t = 40$ min) imposing the steady salt concentration gradient. The white dashed lines represent the channel boundaries, and the solid lines indicate the width, $w_c(t)$, of the fluorescent colloidal stream. (e) Normalised fluorescence intensity profiles along the transverse direction, corresponding to the micrographs in panel (d).

as the total flow rate, $2 \times 12.5 = 25$ μL/min, divided by the channel cross-section area, $w \times h = 400 \times 45 = 2000\ \mu m^2$. The inner solution, seeded with fluorescent colloidal nanoparticles, had a lower LiCl salt concentration $c_L = 0.1$ mM, and it was pumped through the central inlet of the microfluidic device. The outer flow was particle-free and it could be switched between a lower, c_L, and a higher, $c_H = 10$ mM LiCl, salt solution by means of a flow switching valve. Figure 4b shows the schematic of the microdevice, fitted with a flat silicon substrate, together with the imaging acquisition system adopted to investigate the dynamics of fluorescent colloidal particles in the microchannels.

The distribution of silica nanoparticles in the microchannel with and without

a salt concentration gradient, is shown in in Figure 5. The outer stream consisted of a 1mM TRIS buffer (pH = 9) and low (c_L) salt solution seeded with silica nanoparticles at a concentration of $n_0 = 0.005\%$ v/v. TRIS buffer has a dissociation constant of approximately 8.1 at 25°C and it is an effective buffer in the range of pH 7-9 [31]. Thus, TRIS buffer allows to stabilise the surface charge of silica particles and maintains the particle zeta potential to the desired value [27]. The outer stream was also a 1mM TRIS buffer (pH=9) solution, but its salt concentration was varied over time between c_L and c_H, as shown in Figure 5c. The time evolution of the fluorescent colloid distribution within the channel is shown by the epi-fluorescence micrographs in Figure 5d. The micrographs were acquired at a distance of 10 mm from the junction, i.e. at z/w=25, where z is the longitudinal distance from the channel junction. In Figure 5, $t = 0$ is an arbitrarily chosen time after flow stabilisation. By imposing a salt concentration gradient at time $t > 5$ min, the colloidal particles spread spontaneously from the centre towards the outer regions of the channel and accumulated at two symmetric focusing regions at the edges of the colloid flow stream, namely $x/w \simeq \pm 0.25$, where x is the transverse distance from the centre of the channel. The width, $w_c(t)$, of the fluorescent colloidal stream increased from 200 µm to 240 µm. The homogeneous particle distribution within the central region of the channel was recovered when the salt concentration gradient was removed ($t > 15$ min). The time evolution of the fluorescence intensity profiles along the channel transverse direction, x, is shown in Figure 5e. The fluorescence intensity I, which is proportional to the particle concentration n, is normalised with respect to the fluorescence intensity I_0 of the colloidal solution injected in the inner channel of the device. The transverse distance x is also normalised with respect to the channel width w. The fluorescence intensity profile in presence of salt concentration gradient (red curve) was wider than the one in absence of a salt concentration gradient (blue curves), because of the diffusiophoresis velocity, $\mathbf{v}_{DP} = \Gamma_{DP} \nabla c/c$, that drives the nanoparticles from the inner low salt concentration region to the outer high salt concentration regions – with $\Gamma_{DP} > 0$ being the diffusiophoresis coefficient. The non-linear scaling $\mathbf{v}_{DP} \propto \nabla c/c$ results in a diffusiophoresis velocity $\mathbf{v}_{DP}$ decreasing from the centre (low salt) towards the outer (high salt) regions of the channel [27]. Consequently, two symmetric particle focusing peaks appeared at the interface between the inner and outer streams, while the colloid concentration in the central region of the channel decreased. These observations are in agreement with those reported by Abecassis et al. [27, 28], who investigated the spreading and focusing of 200 nm silica particles under the same flow conditions, but in composite PDMS-glass flow focusing junction devices. Interestingly, in these previous studies no diffusioosmosis flow [25], dragging colloids from high to low salt regions, could be observed. Since our devices were made of hydrophilic (silicon and NOA-81) rather than hydrophobic (PDMS) materials, it can be expected that the channel walls had a non-negligible zeta potential, which could lead to the onset of a diffusioosmosis flow with a wall slip velocity, $\mathbf{v}_{DO} = -\Gamma_{DO} \nabla c/c$, with Γ_{DO} the diffusioosmosis coefficient. However, under the examined experimental conditions, no diffusioosmosis flows dragging particles from high to low salt regions

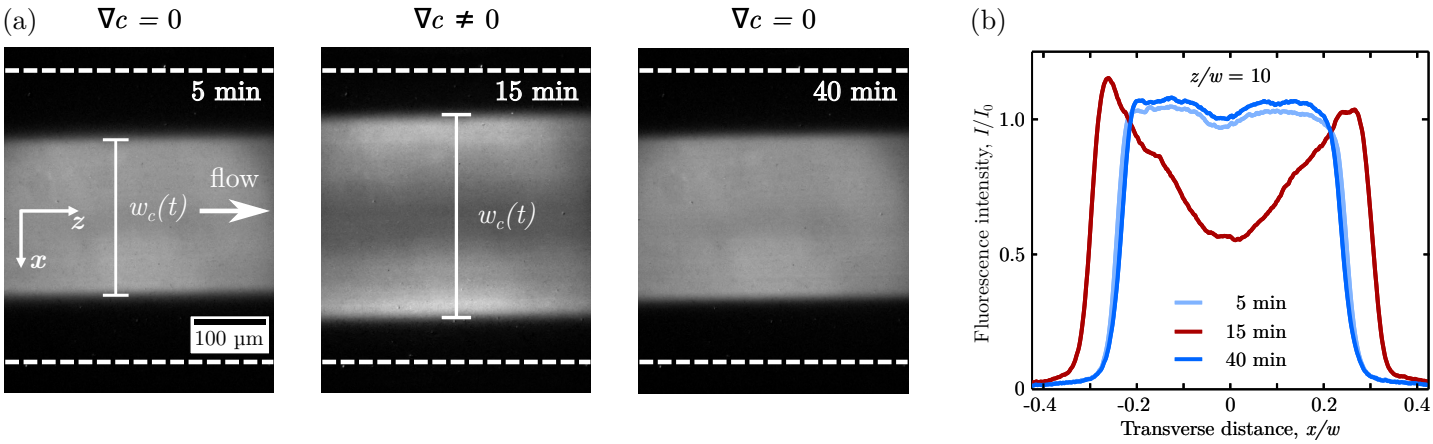

Figure 6: Diffusiophoresis-driven focusing of 200 nm diameter polystyrene particles (0.005% v/v) in a NOA-81 Ψ-junction device with a flat silicon surface. (a) Epi-fluorescence micrographs of the main channel at 4 mm ($z/w = 10$) downstream of the junction, before ($t = 5$min), during ($t = 15$ min) and after ($t = 40$ min) imposing the steady salt concentration gradient. The white dashed lines represent the channel boundaries. (b) Normalised fluorescence intensity profiles along the transverse direction, corresponding to the micrographs in panel (a). The red (blue) curve corresponds to the presence (absence) of the steady salt concentration gradient, ∇c.

could be seen. Note that this does not imply necessarily that there are no diffusioosmosis flows in the system, but just that they are not intense enough to overcome the particle diffusiophoresis migration from low to high salt regions. Finally, upon removal of the salt concentration gradient, the diffusiophoresis migration of particles ceased and the width of the colloidal intensity profiles, $w_c(t)$, reverted to its original size (Figure 5d,e).

Similar experiments were repeated with polystyrene nanoparticles and the results are showed in Figure 6. The inner stream consisted of a DI water suspension of polystyrene nanoparticles at low c_L salt concentration, whereas the outer stream was a DI water solution with a salt concentration varied over time between c_L and c_H. The time evolution of the colloid distribution in a flat silicon device is also shown in Figure 6. At a distance of 4 mm from the junction (i.e. $z/w = 10$), the width $w_c(t)$ of the fluorescent colloidal stream increased from 200 µm to 250 µm upon imposition of the steady salt concentration gradient. Compared to the silica nanoparticle experiments, the larger expansion of the colloidal stream at a closer distance from the junction can be explained by the more negative zeta potential of polystyrene nanoparticles ($\zeta = -58.5 \pm 1$ mV) compared to the one of silica nanoparticles ($\zeta = -41.7 \pm 4$ mV). This results in a higher diffusiophoresis coefficient Γ_{DP}, and thus a larger diffusiophoresis velocity, $\mathbf{v}_{DP}$, which led to a wider particle spreading. It can be concluded that, for a given salt concentration gradient, a higher surface charge of the nanoparticles results in a wider particle spreading over flat silicon substrates. Potentially, such a behaviour could be exploited for the characterisation of nanoparticle

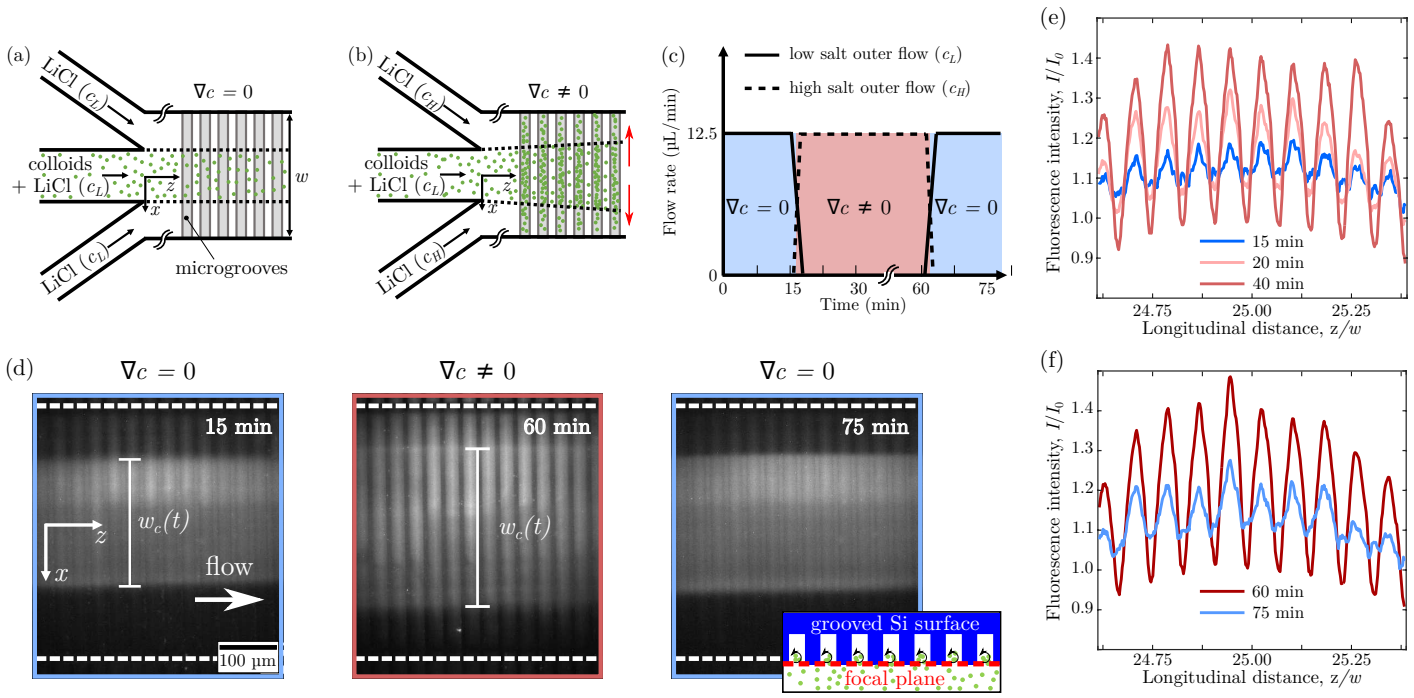

Figure 7: Diffusiophoresis-driven accumulation of 200 nm diameter silica particles (0.05% v/v) in the microgrooves of a NOA-81 Ψ-junction device. (a-b) Flow configuration in the Ψ-junction device in absence (a) and presence (b) of a steady salt concentration gradient. Red arrows show the direction of the salt concentration gradient. The grey-shaded regions corresponds to the microgrooves in the silicon substrate. (c) Time-evolution of the flow rates of the low and high salt outer streams, achieved via the flow switching valve. The red (blue) shaded regions correspond to the presence (absence) of the steady salt concentration gradient, ∇c. (d) Epi-fluorescence micrographs of the main channel at 10 mm ($z/w = 25$) downstream of the junction, before ($t = 15$ min), during ($t = 60$ min) and after ($t = 75$ min) imposing the steady salt concentration gradient. The white dashed lines represent the channel boundaries. (e-f) Time evolution of the normalised fluorescence intensity profiles along the longitudinal direction. The profiles are calculated by averaging the intensity along the transverse direction. Red (blue) curves correspond to the presence (absence) of the salt concentration gradient.

zeta potential by relating the latter with particle spreading via a calibration procedure.

3.3. Particle accumulation in microgrooved substrates

In these experiments, NOA-81 devices fitted with a microgrooved surface were used, as shown schematically in Figure 4c. In a previous study [29], we introduced a microfluidic strategy for the rapid and steady accumulation of nanoparticles within the 8 μm thick grooves of a microstructured silicon surface. Here, we adopted the same strategy, but microstructured silicon surfaces with 24 μm thick grooves were used instead. The results for silica nanoparticles are reported in Figure 7. The inner and outer streams are identical to those used

in the experiments with the flat substrate devices. However, to improve the signal-to-noise ratio of the epi-fluorescence micrographs, the initial concentration of silica nanoparticles in the inner stream, n_0, was increased to 0.05% v/v. The time evolution of the outer stream flow rates is shown in Figure 7c. As in previous experiments, $t = 0$ is an arbitrarily chosen time after flow stabilisation, but before the imposition of the salt concentration gradient. Figure 7d shows the epi-fluorescence micrographs of the device at 10 mm downstream of the junction ($z/w = 25$) under varying flow arrangements for salt solutions. The micrographs were acquired with the focal plan of the microscope objective located at the entrance of the surface grooves, as shown in the inset of Figure 7d. The depth of field of the microscope (namely, the thickness of the slice region that is in acceptably sharp focus in the micrographs) can be estimated [32] as $d = n\,\lambda_{em}/NA^2 + n\,e/(M \cdot NA) \simeq 10$ µm, where $n = 1$ is the refractive index of the objective immersion medium (air), $\lambda_{em} = 510$ nm is the nanoparticle emission wavelength, $e = 4.8$ µm is the pixel pitch of the CMOS camera, $NA = 0.25$ and $M = 10$ are the objective numerical aperture and magnification, respectively. As a result, the micrographs captured the fluorescence intensity of nanoparticles located either in the main channel or inside the microgrooves, at few microns from the groove entrance. As expected, in absence of a salt concentration gradient ($t < 15$ min), the colloids remained evenly distributed in the central region of the channel (Figure 7d). Upon injection of the higher salt outer stream ($t > 15$ min), a steady salt concentration gradient was generated in the transverse direction (red arrows in Figure 7b), leading to colloid spreading along the same direction (i.e. wider w_c) as it occurred in the case of the flat silicon substrate. As previously reported [29], a component of the salt concentration gradient along the channel depth direction is originated by the Poiseuille-like velocity profile in the rectangular channel. This component leads to the diffusiophoresis migration of colloids from the channel bulk into the grooves, as confirmed by the micrograph at $t = 60$ min showing brighter transverse regions corresponding to the locations of the surface microgrooves. Differently from what was previously observed in $T = 8$ µm thick microgrooves, for the examined surface ($T = 24$ µm) the colloids were homogeneously distributed inside the grooves along the transverse (x) direction. More interestingly, the colloids inside the grooves migrated towards the outer stream regions and spread well beyond the width, $w_c(t)$, of the fluorescent colloidal stream. Our previous study [29] demonstrated that particle accumulation results from the combined effects of diffusiophoresis transport and hydrodynamic flow recirculation within the grooves. Thus, it can be expected that a change in groove thickness affects the flow field within the grooves and, consequently, the particle distribution therein. As the outer stream was switched back to the lower salt solution, the effect of particle accumulation within the grooves disappeared and the initial particle distribution within the channel was recovered ($t = 75$ min). Figure 7e-f show the time evolution of the normalised fluorescence intensity profile along the flow (longitudinal) direction, z. It can be observed that without salt concentration gradient (blue curve), the intensity profile had an oscillating trend with a wavelength matching the groove pitch, $L = 24$ µm. It is hypothes-

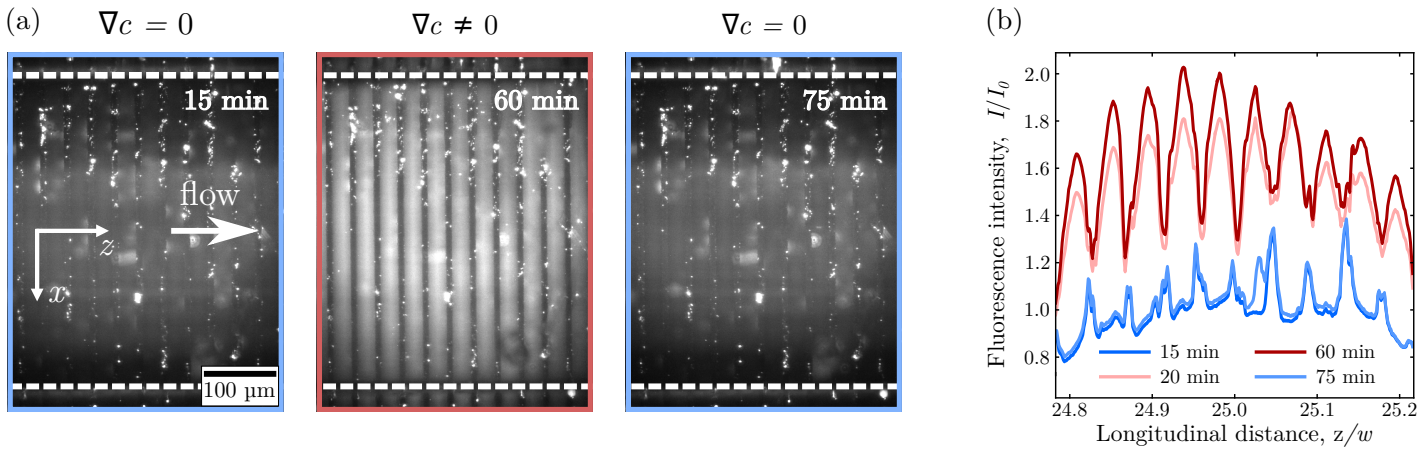

Figure 8: Diffusiophoresis-driven accumulation of 200 nm diameter polystyrene particles (0.05% v/v) in the microgrooves of a NOA-81 Ψ-junction device. (a) Epi-fluorescence micrographs of the main channel at 10 mm ($z/w = 25$) downstream of the junction, before ($t = 15$ min), during ($t = 60$ min) and after ($t = 75$ min) imposing the steady salt concentration gradient. The white dashed lines represent the channel boundaries. (b) Time evolution of the normalised fluorescence intensity profiles along the longitudinal direction. The profiles are calculated by averaging the intensity along the transverse direction. Red (blue) curves correspond to the presence (absence) of the steady salt concentration gradient, ∇c.

ised that, in the absence of a salt concentration gradient, particles could enter the groove by advection along the flow streamlines that formed a recirculation region at the groove entrance — see inset in Figure 7d. However, particles could not travel further down the grooves due to their low diffusivity. As a result, there is a correlation between the peaks of the fluorescence intensity profile and the groove locations. For $t > 15$ min, the salt concentration gradient caused the accumulation of particles within the grooves, as demonstrated by the higher peaks in the corresponding intensity profiles (red curves). A steady-state distribution of particles within the grooves was achieved ca. 20 min after the outer flow was switched and the salt concentration gradient was imposed. Particles could diffuse out of the grooves once the salt concentration gradient was removed, as confirmed by the intensity profile at $t = 75$ min. These results demonstrated that the particle trapping and accumulation phenomenon is fully reversible.

Similar experiments were repeated with the polystyrene nanoparticles and the corresponding results are showed in Figure 8. Again, the inner and outer streams were identical to those used in the experiments with the flat substrate devices, but the initial concentration of particles in the inner stream, n_0, was increased to 0.05% v/v. As it can be expected, the higher diffusiophoresis coefficient of polystyrene colloids resulted in a more intense accumulation of nanoparticles within the grooves of the structured silicon surface, as shown by the fluorescence micrographs and intensity profiles in Figure 8. Consequently, also this particle manipulation strategy could be exploited potentially for the characterisation of colloid zeta potential, once the intensity of the focusing peak

is correlated to the particle zeta potential via calibration.

3.4. Synthesis of liposomes

In this last set of experiments, NOA flow focusing devices fitted with a flat silicon substrate were used to generate chemical concentration gradients between an aqueous and alcohol phase to synthesise nanoscale lipid vesicles according to the hydrodynamic focusing procedure introduced by Jahn et al. [21]. The synthesis of liposomes by hydrodynamic focusing has been previously reported in glass capillaries [33, 34] as well as PDMS [35, 36] and glass [37] flow focusing junction devices. This approach has also been adopted for the concurrent loading of hydrophilic or hydrophobic drugs, dispersed either in the aqueous or alcohol phase, respectively [38]. It is worth noting that the excellent chemical resistance of glass devices allows for a wider selection of solvents that can be used for the lipid and hydrophobic drug solutions, compared to PDMS devices. However, the manufacturing of glass flow focusing devices is more complicated and expensive than PDMS chips. NOA flow focusing devices, instead, combine good chemical resistance with easy and cost-effective fabrication procedures. To date, only one study [24] demonstrated the formation of liposomes using a composite NOA-polystyrene flow focusing device. However, the device geometry was rather complex, including seven converging inlet channels and an array of staggered herringbones on the side of the main channels to promote micromixing. In this study, we demonstrate that a composite NOA-silicon flow focusing device with a plain Ψ-junction geometry is sufficient to produce liposome population with a controlled narrow size distribution.

In these experiments, the outer streams consisted of a buffer aqueous solution, containing 5 μM EDTA, 5 μM HEPES and 0.01 mM LiCl, whereas the inner stream was an ethanol solution with DOPC lipids at a concentration of 15 mg/mL. A schematic of the flow configuration is shown in Figure 9a. Under these conditions, ethanol and lipid molecules diffuse into the buffer solution while the water molecules diffuse into the alcohol phase. As the solubility limit of the lipids is exceeded, they self-assemble into disk-like bilayered lipid fragments. These flat lipid structures grow and bend until they form stable closed vesicles at the interface between the two phases [39, 40]. In our experiments, the flow rate of the outer stream, Q_o, was kept at 50 μL/min, and the ratio between the outer and inner flow rates, Q_o/Q_i, was varied between 5 and 50. The corresponding average flow velocities, U_{av}, varied between 56 mm/s and 47 mm/s. It is worth noting that full mixing between phases occurs when the thickness of the interfacial diffusion layer between the two phases, $\delta(z)$, matches half the width of the inner channel $w_i = 100\,\mu\text{m}$ (Figure 9a). In the bulk of the rectangular microchannel, namely away from the top and bottom walls, the function $\delta(z)$ can be approximated as $\delta(z) \simeq \sqrt{D_{eth}\, z/U_{av}}$, where $D_{eth} = 0.89 \times 10^{-9}\,\text{m}^2/\text{s}$ is the diffusion coefficient of ethanol in water [41]. Conversely, near the top and bottom walls of the device, $\delta(z) \simeq (D_{eth}\, zh/U_{av})^{1/3}$, due to the Poiseuille-like velocity profile along the channel depth direction [42]. It follows that at the outlet of the device ($z = 25$ mm), the thickness of the diffusion layer is 21 μm

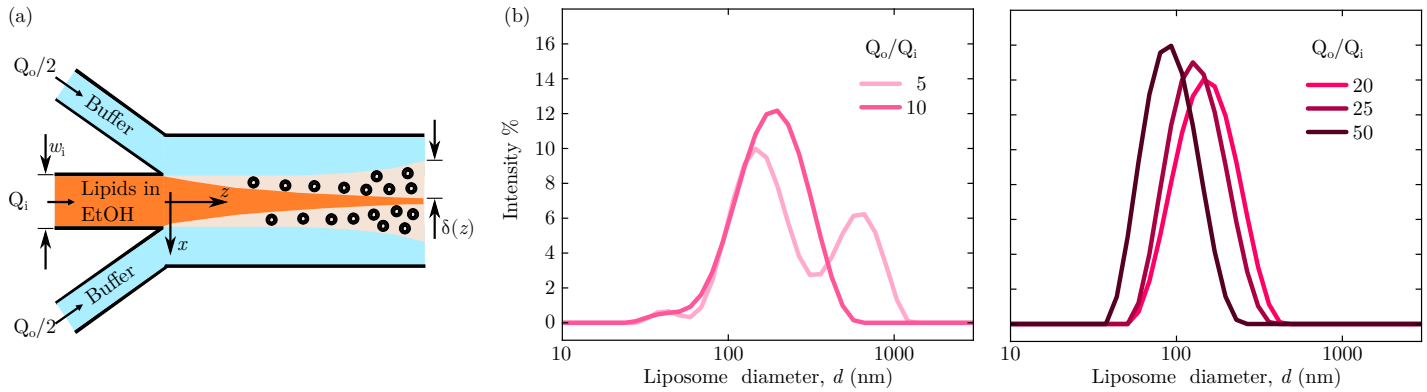

Figure 9: Synthesis of DOPC liposomes by hydrodynamic focusing. (a) Schematic of the NOA Ψ-junction device fitted with a flat silicon substrate. The inner lipid-ethanol stream, with a flow rate Q_i, is hydrodynamically focused by the outer buffer stream, with a flow rate Q_o. (b) Size distribution of liposomes generated under varying flow rate ratios, Q_o/Q_i. The Z-average particle sizes, $\bar{d}$, and polydispersity index, PDI, are i) $Q_o/Q_i = 5$, $\bar{d} = 259 \pm 11$ nm, $PDI = 0.462$ ii) $Q_o/Q_i = 10$, $\bar{d} = 160 \pm 3$ nm, $PDI = 0.182$ iii) $Q_o/Q_i = 20$, $\bar{d} = 141 \pm 4$ nm, $PDI = 0.082$ iv) $Q_o/Q_i = 25$, $\bar{d} = 127 \pm 1$ nm, $PDI = 0.176$ v) $Q_o/Q_i = 50$, $\bar{d} = 88 \pm 2$ nm, $PDI = 0.144$.

and 28 µm in the bulk and near the walls, respectively. This is only 20% of inner channel width, hence full mixing is not achieved in the device.

The resulting liposome distribution for varying flow rate ratios are reported in Figure 9b. At low flow rate ratios and, thus, low shear forces, liposomes can aggregate into clusters and bilayer defects may induce the fusion of adjacent liposomes [43]. This mechanism could explain the observation of two peaks in the particle size distribution at the lowest flow ratio $Q_o/Q_i = 5$. At higher flow rate ratios, a single population of particle size distribution can be achieved, suggesting that liposome aggregation and fusion is no longer occurring under these shear stress conditions. It can also be observed that the average liposome size decreases with increasing flow rate ratios, in agreement with previous studies [39, 44, 43]. To conclude, composite NOA-silicon flow junction devices can be used successfully to generate liposome population with a narrow size distribution that can be controlled by adjusting the ratio between the flow rates of the buffer and alcohol streams.

4. Conclusions

NOA microfluidic devices, manufactured via microfluidic sticker technique, provide an effective alternative option to PDMS devices due to their many advantages, including improved optical transparency, chemical resistance to many organic solvents, gas impermeability, and high mechanical stiffness. In this study, we reported the optimised protocol for the fabrication of composite NOA 81-silicon devices with a flow focusing junction. The devices fitted

with flat silicon substrates were used to generate steady-state salt concentration gradients to achieve the spreading and focusing of silica and polystyrene nanoparticles. Wider spreading toward the high salt concentration regions was observed for the particles (polystyrene) with a more negative zeta potential. Despite the hydrophilic NOA and silicon walls of the channels bear a negative surface charge, diffusioosmosis flows dragging the colloids from high to low salt regions could not be detected, hence confirming that particle diffusiophoresis is the main mechanism governing the particle dynamics. These observations are in agreement with previously reported particle spreading experiments in composite hydrophobic PDMS/hydrophilic glass devices [27]. We also demonstrated the accumulation of silica and polystyrene particles within the grooves of NOA flow focusing devices fitted with silicon microgrooved substrates. In a previous study, we showed that, for 8 μm thick grooves, particles accumulated at the centre of the channel, while here we demonstrated that, for 24 μm thick grooves, particles are evenly accumulated within the groove along the whole channel width. This is probably due to the fact that the groove thickness affects the hydrodynamic flow field, which in turn determines the particle distribution within the grooves. Furthermore, our experimental observations led us to conclude that particles (polystyrene) with a more negative zeta potential tends to get more concentrated within the device grooves, thereby suggesting a potential strategy for the characterisation of particle zeta potential based on the fluorescence intensity of the accumulation peaks within the grooves. Finally, we showed that composite NOA-silicon flow focusing devices with a Ψ-junction can be successfully used for the synthesis of DOPC liposomes with a narrow size distribution controlled by the flow rate ratio between the hydrodynamically focused streams. In conclusions, this study showcases the potential of NOA flow focusing devices for the synthesis and manipulation of nanoparticles, which could underpin a variety of microfluidic applications, such as drug synthesis and encapsulation, bioanalysis, nanoparticle characterisation and filtration.

Acknowledgements

This research was supported by the EPSRC (EP/S013865/1) and the Santander Mobility Grant awarded to NS.

References

[1] B. K. Gale, A. R. Jafek, C. J. Lambert, B. L. Goenner, H. Moghimifam, U. C. Nze, S. K. Kamarapu, A review of current methods in microfluidic device fabrication and future commercialization prospects, Inventions 3 (3) (2018) 60.

[2] A. Manz, D. J. Harrison, E. M. Verpoorte, J. C. Fettinger, A. Paulus, H. Lüdi, H. M. Widmer, Planar chips technology for miniaturization and

integration of separation techniques into monitoring systems: capillary electrophoresis on a chip, Journal of Chromatography A 593 (1-2) (1992) 253–258.

[3] D. R. Reyes, D. Iossifidis, P.-A. Auroux, A. Manz, Micro total analysis systems. 1. introduction, theory, and technology, Analytical Chemistry 74 (12) (2002) 2623–2636.

[4] G. M. Whitesides, The origins and the future of microfluidics, nature 442 (7101) (2006) 368–373.

[5] S. D. Senturia, Microsystem design, Springer Science & Business Media, 2007.

[6] C. Iliescu, H. Taylor, M. Avram, J. Miao, S. Franssila, A practical guide for the fabrication of microfluidic devices using glass and silicon, Biomicrofluidics 6 (1) (2012) 016505.

[7] R. Al Nuumani, G. Bolognesi, G. T. Vladisavljevic, Microfluidic production of poly (1, 6-hexanediol diacrylate)-based polymer microspheres and bifunctional microcapsules with embedded tio2 nanoparticles, Langmuir 34 (39) (2018) 11822–11831.

[8] R. Al Nuumani, S. K. Smoukov, G. Bolognesi, G. T. Vladisavljevic, Highly porous magnetic janus microparticles with asymmetric surface topology, Langmuir 36 (42) (2020) 12702–12711.

[9] T. Deydier, G. Bolognesi, G. T. Vladisavljević, Scaled-up droplet generation in parallelised 3d flow focusing junctions, Colloids and Surfaces A: Physicochemical and Engineering Aspects 641 (2022) 128439.

[10] P. N. Nge, C. I. Rogers, A. T. Woolley, Advances in microfluidic materials, functions, integration, and applications, Chemical Reviews 113 (4) (2013) 2550–2583.

[11] C.-W. Tsao, Polymer microfluidics: Simple, low-cost fabrication process bridging academic lab research to commercialized production, Micromachines 7 (12) (2016) 225.

[12] J. C. McDonald, D. C. Duffy, J. R. Anderson, D. T. Chiu, H. Wu, O. J. Schueller, G. M. Whitesides, Fabrication of microfluidic systems in poly (dimethylsiloxane), Electrophoresis: An International Journal 21 (1) (2000) 27–40.

[13] J. C. McDonald, G. M. Whitesides, Poly (dimethylsiloxane) as a material for fabricating microfluidic devices, Accounts of Chemical Research 35 (7) (2002) 491–499.

[14] D. Bartolo, G. Degré, P. Nghe, V. Studer, Microfluidic stickers, Lab on a Chip 8 (2) (2008) 274–279.

[15] T. Fu, Y. Wu, Y. Ma, H. Z. Li, Droplet formation and breakup dynamics in microfluidic flow-focusing devices: From dripping to jetting, Chemical Engineering Science 84 (2012) 207–217.

[16] L. Martín-Banderas, M. Flores-Mosquera, P. Riesco-Chueca, A. Rodríguez-Gil, Á. Cebolla, S. Chávez, A. M. Gañán-Calvo, Flow focusing: a versatile technology to produce size-controlled and specific-morphology microparticles, Small 1 (7) (2005) 688–692.

[17] S.-Y. Teh, R. Lin, L.-H. Hung, A. P. Lee, Droplet microfluidics, Lab on a Chip 8 (2) (2008) 198–220.

[18] G. Bolognesi, A. Hargreaves, A. D. Ward, A. K. Kirby, C. D. Bain, O. Ces, Microfluidic generation of monodisperse ultra-low interfacial tension oil droplets in water, RSC Advances 5 (11) (2015) 8114–8121.

[19] M. Lu, A. Ozcelik, C. L. Grigsby, Y. Zhao, F. Guo, K. W. Leong, T. J. Huang, Microfluidic hydrodynamic focusing for synthesis of nanomaterials, Nano Today 11 (6) (2016) 778–792.

[20] M. Rhee, P. M. Valencia, M. I. Rodriguez, R. Langer, O. C. Farokhzad, R. Karnik, Synthesis of size-tunable polymeric nanoparticles enabled by 3d hydrodynamic flow focusing in single-layer microchannels, Advanced Materials 23 (12) (2011) H79–H83.

[21] A. Jahn, W. N. Vreeland, M. Gaitan, L. E. Locascio, Controlled vesicle self-assembly in microfluidic channels with hydrodynamic focusing, Journal of the American Chemical Society 126 (9) (2004) 2674–2675.

[22] A. Zizzari, L. Carbone, M. Cesaria, M. Bianco, E. Perrone, F. Rendina, V. Arima, Continuous flow scalable production of injectable size-monodisperse nanoliposomes in easy-fabrication milli-fluidic reactors, Chemical Engineering Science 235 (2021) 116481.

[23] H. Aghaei, A. R. Solaimany Nazar, Continuous production of the nanoscale liposome in a double flow-focusing microfluidic device, Industrial & Engineering Chemistry Research 58 (51) (2019) 23032–23045.

[24] D. Witzigmann, S. Sieber, F. Porta, P. Grossen, A. Bieri, N. Strelnikova, T. Pfohl, C. Prescianotto-Baschong, J. Huwyler, Formation of lipid and polymer based gold nanohybrids using a nanoreactor approach, RSC Advances 5 (91) (2015) 74320–74328.

[25] J. L. Anderson, Colloid transport by interfacial forces, Annual Review of Fluid Mechanics 21 (1) (1989) 61–99.

[26] S. Shin, Diffusiophoretic separation of colloids in microfluidic flows, Physics of Fluids 32 (10) (2020) 101302.

[27] B. Abécassis, C. Cottin-Bizonne, C. Ybert, A. Ajdari, L. Bocquet, Boosting migration of large particles by solute contrasts, Nature materials 7 (10) (2008) 785–789.

[28] B. Abécassis, C. Cottin-Bizonne, C. Ybert, A. Ajdari, L. Bocquet, Osmotic manipulation of particles for microfluidic applications, New Journal of Physics 11 (7) (2009) 075022.

[29] N. Singh, G. T. Vladisavljević, F. Nadal, C. Cottin-Bizonne, C. Pirat, G. Bolognesi, Reversible trapping of colloids in microgrooved channels via diffusiophoresis under steady-state solute gradients, Physical Review Letters 125 (24) (2020) 248002.

[30] R. J. Hunter, Foundations of colloid science, Oxford University Press, 2001.

[31] A. Sikora, D. Bartczak, D. Geißler, V. Kestens, G. Roebben, Y. Ramaye, Z. Varga, M. Palmai, A. G. Shard, H. Goenaga-Infante, et al., A systematic comparison of different techniques to determine the zeta potential of silica nanoparticles in biological medium, Analytical Methods 7 (23) (2015) 9835–9843.

[32] B. E. Saleh, M. C. Teich, Fundamentals of photonics, john Wiley & Sons, 2019.

[33] G. T. Vladisavljević, A. Laouini, C. Charcosset, H. Fessi, H. C. Bandulasena, R. G. Holdich, Production of liposomes using microengineered membrane and co-flow microfluidic device, Colloids and Surfaces A: Physicochemical and Engineering Aspects 458 (2014) 168–177.

[34] R. Othman, G. T. Vladisavljević, H. H. Bandulasena, Z. K. Nagy, Production of polymeric nanoparticles by micromixing in a co-flow microfluidic glass capillary device, Chemical Engineering Journal 280 (2015) 316–329.

[35] L. Jiang, W. Wang, Y. Chau, S. Yao, Controllable formation of aromatic nanoparticles in a three-dimensional hydrodynamic flow focusing microfluidic device, RSC Advances 3 (39) (2013) 17762–17769.

[36] R. Hood, W. Vreeland, D. L. DeVoe, Microfluidic remote loading for rapid single-step liposomal drug preparation, Lab on a Chip 14 (17) (2014) 3359–3367.

[37] F. Roffo, A. M. Ponsiglione, P. A. Netti, E. Torino, coupled hydrodynamic flow focusing (chff) to engineer lipid–polymer nanoparticles (lipons) for multimodal imaging and theranostic applications, Biomedicines 10 (2) (2022) 438.

[38] W.-Z. S. Lin, N. Malmstadt, Liposome production and concurrent loading of drug simulants by microfluidic hydrodynamic focusing, European Biophysics Journal 48 (6) (2019) 549–558.

[39] A. Jahn, F. Lucas, R. A. Wepf, P. S. Dittrich, Freezing continuous-flow self-assembly in a microfluidic device: toward imaging of liposome formation, Langmuir 29 (5) (2013) 1717–1723.

[40] M. Maeki, Y. Fujishima, Y. Sato, T. Yasui, N. Kaji, A. Ishida, H. Tani, Y. Baba, H. Harashima, M. Tokeshi, Understanding the formation mechanism of lipid nanoparticles in microfluidic devices with chaotic micromixers, PLoS One 12 (11) (2017) e0187962.

[41] E. L. Cussler, E. L. Cussler, Diffusion: mass transfer in fluid systems, Cambridge University Press, 2009.

[42] R. F. Ismagilov, A. D. Stroock, P. J. Kenis, G. Whitesides, H. A. Stone, Experimental and theoretical scaling laws for transverse diffusive broadening in two-phase laminar flows in microchannels, Applied Physics Letters 76 (17) (2000) 2376–2378.

[43] M. V. Bandulasena, G. T. Vladisavljević, B. Benyahia, Versatile reconfigurable glass capillary microfluidic devices with lego® inspired blocks for drop generation and micromixing, Journal of Colloid and Interface Science 542 (2019) 23–32.

[44] A. Jahn, S. M. Stavis, J. S. Hong, W. N. Vreeland, D. L. DeVoe, M. Gaitan, Microfluidic mixing and the formation of nanoscale lipid vesicles, ACS Nano 4 (4) (2010) 2077–2087.

Declaration of interests

☒The authors declare that they have no known competing financial interests or personal relationships that could have appeared to influence the work reported in this paper.

☐The authors declare the following financial interests/personal relationships which may be considered as potential competing interests: